Layer-Controlled, Wafer-Scale, and Conformal Synthesis of Tungsten Disulfide Nanosheets Using Atomic Layer Deposition

Jeong-Gyu Song,[†,‡] Jusang Park,[†,‡] Wonseon Lee,[‡] Taejin Choi,[‡] Hanearl Jung,[‡] Chang Wan Lee,[‡] Sung-Hwan Hwang,[§] Jae Min Myoung,[§] Jae-Hoon Jung,[∥] Soo-Hyun Kim,[∥] Clement Lansalot-Matras,[⊥] and Hyungjun Kim[*,‡]

[‡]School of Electrical and Electronics Engineering and [§]Department of Materials Science and Engineering, Yonsei University, Seoul 120-749, Korea, [∥]School of Materials Science and Engineering, Yeungnam University, Gyeongsan-si 712-749, Korea, and [⊥]Air Liquide Laboratories Korea, Yonsei Engineering Research Park, 50 Yonsei-ro, Seodaemun-gu, Seoul, 120-749, Korea. [†]These authors contributed equally (J.-G.S. and J.P.).

ABSTRACT The synthesis of atomically thin transition-metal disulfides (MS_2) with layer controllability and large-area uniformity is an essential requirement for their application in electronic and optical devices. In this work, we describe a process for the synthesis of WS_2 nanosheets through the sulfurization of an atomic layer deposition (ALD) WO_3 film with systematic layer controllability and wafer-level uniformity. The X-ray photoemission spectroscopy, Raman, and photoluminescence measurements exhibit that the ALD-based WS_2 nanosheets have good stoichiometry, clear Raman shift, and bandgap dependence as a function of the number of layers. The electron mobility of the monolayer WS_2 measured using a field-effect transistor (FET) with a high-k dielectric gate insulator is shown to be better than that of CVD-grown WS_2, and the subthreshold swing is comparable to that of an exfoliated MoS_2 FET device. Moreover, by utilizing the high conformality of the ALD process, we have developed a process for the fabrication of WS_2 nanotubes.

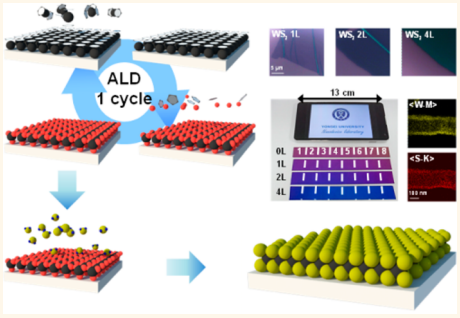

KEYWORDS: WS_2 · transition-metal dichalcogenides · two-dimensional materials · atomic layer deposition · WS_2 nanotube

Transition-metal dichalcogenides (TMDCs) are layered materials with strong in-plane covalent bonding and weak out-of-plane van der Waals bonding. These materials have attracted significant attention due to their immense potential for use in various applications.[1−4] Among various TMDCs, one- and two-dimensional (1D and 2D) transition-metal disulfides (TMSs), MS_2 (M = W, Mo), have been intensively studied to examine their properties, including their electrical transport[5−8] and structure,[9−11] luminescence,[12−14] photocurrent,[15−17] magnetism,[18,19] battery-electrode,[20−23] and catalytic[24] properties, as well as their strain effects[19,25,26] and valley polarization.[27,28] In particular, 2D atomically thin MS_2 nanosheets exfoliated from bulk MS_2 have shown exotic electronic and optical properties, such as indirect-to-direct bandgap transition with reducing number of layers, high carrier mobility (approximately 200 $cm^2/V \cdot s$) and strong spin−orbit coupling due to their broken inversion symmetry.[5,12,25,28−30] Thus, atomically thin MS_2 nanosheets are expected to be widely used in the electronics field[31−33] and in optical applications.[2,14,15,27,28,34,35]

The need to synthesize high-quality MS_2 nanosheets with controllable thickness and wafer-scale uniformity to overcome the limitations of the exfoliation method, such as isolation, small size (on the order of a few micrometers), and low productivity, is immense. Recently, attempts have been made to satisfy these needs *via* the synthesis of atomically thin MS_2 nanosheets by liquid exfoliation,[13,36] annealing $(NH_4)_2MoS_4$ films,[37] chemical vapor deposition (CVD) using WO_3 and MoO_3 with sulfur powder[38−41] and sulfurization of metal[42] or metal-oxide films.[12,43,44] In particular, monolayer MS_2 nanosheets were synthesized by CVD[38−41] and sulfurization of WO_3 method.[12,44] However, previously reported methods have several limitations, such as difficulties in systematical

* Address correspondence to hyungjun@yonsei.ac.kr.

Received for review October 5, 2013 and accepted November 19, 2013.

Published online November 19, 2013
10.1021/nn405194e

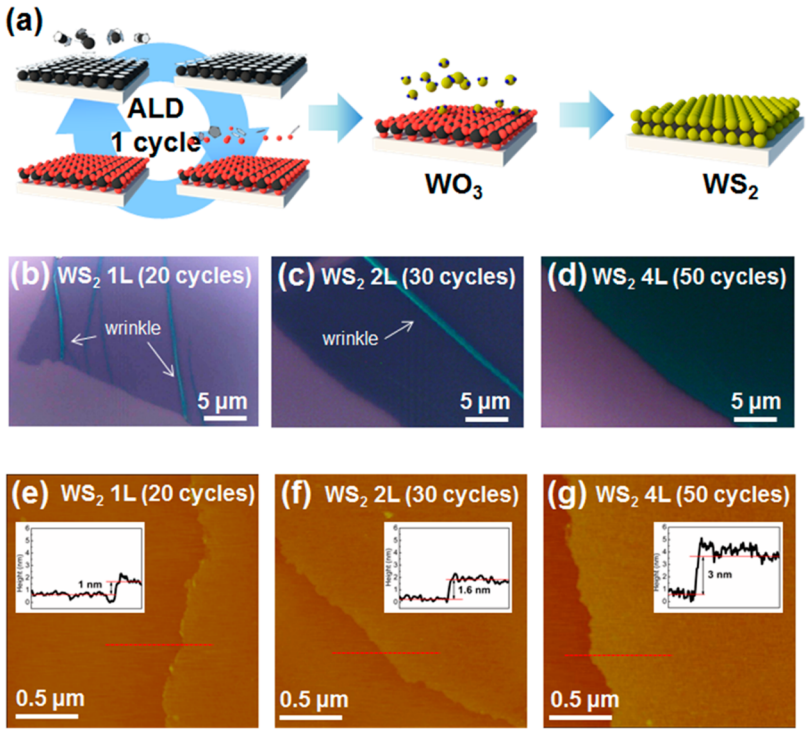

Figure 1. (a) Synthesis procedure for the ALD-based WS_2 nanosheets, (b, c, and d) OM images of the transferred WS_2 nanosheet on the SiO_2 substrate for the mono-, bi-, and tetralayered thicknesses, respectively, and (e, f, and g) AFM images and height profiles (inset) of the transferred WS_2 nanosheet on the SiO_2 substrate for the mono-, bi-, and tetralayered thicknesses, respectively.

control of the thickness and limited wafer-scale uniformity. Moreover, the literature contains few reports on the synthesis of WS_2 nanosheets and less than that of MoS_2. Therefore, an improved synthesis process for atomically thin WS_2 nanosheets with systematic thickness controllability and wafer scale uniformity is required.

In this report, we describe a novel synthesis method of WS_2 nanosheets on SiO_2 substrates by the sulfurization of a WO_3 film prepared by atomic layer deposition (ALD). Because ALD is utilized for the deposition of the WO_3, the synthesized WS_2 layer retains the inherent benefits of the ALD process, which include thickness controllability, reproducibility, wafer-level thickness uniformity, and high conformality.[45,46] In this way, we systematically controlled the number of WS_2 layers (from mono- to multilayers) by controlling the number of cycles of ALD WO_3. We measured the electrical properties of the synthesized monolayer WS_2 nanosheets by fabricating and characterizing a top-gate field-effect transistor (FET) using a high-k dielectric gate insulator. Significantly higher field-effect electron mobility and lower subthreshold swing (SS) than previous reports on synthesized WS_2[40,41] were observed. Furthermore, we fabricated 1D WS_2 nanotubes (WNTs) by sulfurization of ALD WO_3 layer deposited on Si nanowires (NWs). In this way, systematic thickness controllability was realized for WNTs, which could not be achieved in previously reported WNTs synthesis processes.[47,48]

RESULTS AND DISCUSSION

The overall ALD synthesis scheme for the WS_2 nanosheets is illustrated in Figure 1a. The WO_3 films were deposited to the desired thickness on a SiO_2 (285 nm)/Si substrate by plasma-enhanced ALD (PE-ALD) using $WH_2(iPrCp)_2$ (source Air Liquide) and oxygen plasma. Subsequently, the WO_3 deposited on the SiO_2/Si substrate was placed in the center of a tube furnace (1.2 in. in diameter) and sulfurized in Ar and H_2S ambient at high temperatures.

Figure 1(b–d) show optical microscopy (OM) images of the sulfurized WO_3 nanosheets grown over 20, 30, and 50 ALD cycles. The WS_2 nanosheets were transferred to new SiO_2 substrates to confirm the thickness by atomic force microscopy (AFM) similar to a previously reported method.[44] The synthesized WS_2 nanosheets are uniform and continuous with some wrinkles, which are unavoidably formed during the transfer process. Additionally, the apparent colors of the transferred WS_2 nanosheets change from pale green to dark green as the number of PE-ALD WO_3 cycles increases. Figure 1(e–g) represent the measured AFM images of the transferred WS_2 nanosheets. The measured thicknesses of the synthesized WS_2 nanosheets are approximately 1, 1.6, and 3 nm for 20, 30, and 50 ALD cycles, respectively. These thicknesses correspond to mono-, bi-, and tetralayers of WS_2 nanosheets, given that the height of the monolayer WS_2 on SiO_2 is approximately 1 nm and the spacing

between the first and the second WS_2 layers is approximately 0.6 nm.[12] As reported previously, the larger AFM-measured spacing between the first monolayer and the substrate than that between WS_2 layers is due to the effect of distinct tip−sample and tip−substrate interactions.[4,12] The WS_2 nanosheets were not formed by the sulfurization of less than 10 cycles of PE-ALD WO_3 (Figure S2), which is attributed to a nucleation delay during the initial growth of WO_3. After the delay, each WS_2 layer forms after 10 cycles (approximately 1 nm) of the PE-ALD WO_3 process. This observation agrees with a previous report, where approximately 1 nm of a thermally evaporated WO_3 film transform to a monolayer WS_2 *via* sulfurization.[44] Thus, we conclude that we can systematically control the number of layers of WS_2 by controlling the number of PE-ALD WO_3 cycles.

The WS_2 nanosheets were further characterized using Raman, photoluminescence (PL) and X-ray photoemission spectroscopy (XPS). The Raman spectra (λ_{exc} = 633 nm) for the various mono-, bi-, and tetralayer WS_2 nanosheets are shown in Figure 2a. The WS_2 nanosheets exhibit first-order modes at approximately 356 and 420 cm^{-1}, corresponding to the E^1_{2g} and A_{1g} modes from in-plane and out-of-plane vibrations, respectively.[12,44,49] A second-order mode is also observed: the 2LA(M) mode at approximately 350 cm^{-1}. The changes in the relative peak intensity ratios (E^1_{2g}/A_{1g}) and peak distances between the E^1_{2g} and A_{1g} modes depend on the number of layers (mono-, bi-, or tetralayers). To clarify this observation, we fitted the Raman peaks using a Lorentzian function and extracted the peak intensities and positions for the overlapping 2LA(M), E^1_{2g} and A_{1g} modes, depending on the number of layers. Figure 2b shows the relative peak intensity ratio and peak distance as a function of the number of layers. The relative peak intensity ratio increases from 0.55 to 0.8 as the number of layers increased (from mono- to tetralayer nanosheets). The relative peak intensity ratio appeared to be affected primarily by the change in scattering volume.[49] Additionally, the relative peak distance increases from 61.7 to 65 cm^{-1} as the number of layers increased due to an increase in the A_{1g} mode frequency and a decrease in the E^1_{2g} mode frequency. These variations in the Raman frequency of the A_{1g} and E^1_{2g} modes depending on the number of layers can be explained by weak interlayer interactions and the reduced long-range Coulomb interaction between the effective charges caused by an increase in the dielectric screening, respectively.[49,50]

The PL spectra of the WS_2 as a function of the number of layers are shown in Figure 2c. The spectrum of monolayer WS_2 shows a strong PL signal at 2.01 eV, which is consistent with the reported band gap for the monolayer WS_2. A weak and wide PL signal is observed at 1.97 eV for the bilayer WS_2 nanosheet. For the tetralayer WS_2 nanosheet, only a very weak PL signal at near 1.4 eV is observed, which is due to the indirect band gap as previously reported.[12,29,30] The red shift

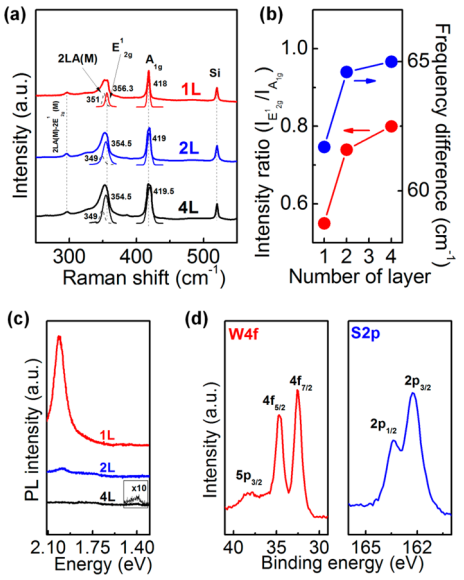

Figure 2. (a) Raman spectra for the mono- (red), bi- (blue), and tetralayer (black) WS_2 nanosheets on SiO_2 substrates, the 2LA(M) (dash) and E^1_{2g} (solid) peaks were deconvoluted using a Lorentzian function, (b) relative Raman peak intensities (red) and peak distances (blue) of the E^1_{2g} and A_{1g} bands for the mono-, bi-, and tetralayer WS_2 nanosheets, (c) PL spectra for the mono- (red), bi- (blue), and tetralayer (black) WS_2 nanosheets on SiO_2 substrates and (d) XPS measurements for the W4f (red) and S2p (blue) core levels of the monolayer WS_2 nanosheet.

and low intensity of the PL signals with increasing number of layers is due to the band gap transition from direct to indirect, which agrees with previous results related to the dependence of the PL signal on the number of layers.[29,30,44] These PL results again confirm the layer controllability for the process scheme described here. The XPS spectra of the monolayer WS_2 at the W4f and S2p core levels are shown in Figure 2d. The W4f core level result shows three peaks at 34.8, 32.6, and 38.2 eV, which correspond to the $W4f_{5/2}$ and $W4f_{7/2}$ levels for the W^{4+} and $W5p_{3/2}$ states, respectively. The S2p core level spectrum exhibits two peaks at 163.4 and 162.3 eV, which are assigned to the doublet $S2p_{1/2}$ and $S2p_{3/2}$. The calculated stoichiometric ratio is 2 (S/W), and all the XPS results agree with the previous reported results for WS_2.[40]

Then, mono-, bi-, and tetralayer WS_2 were synthesized on 2 × 13 cm^2 SiO_2 substrates (Figure 3a) to demonstrate the good uniformity of the current process. It should be noted that the substrate size was limited by the diameter of the tube furnace (1.2 in. diameter with a 15 cm hot-zone length) in the current experiments. The as-grown WS_2 nanosheets show an obvious color dependency on the number of layers. The Raman spectra were measured at eight different positions along the length of the nanosheet to confirm large-area uniformity. The relative Raman peak intensities and distances of the E^1_{2g} and A_{1g} modes are plotted in Figure 3b for each position. The variations in the relative peak intensities as a function of the position are small: between 3 and 0.2% for all the samples. In addition,

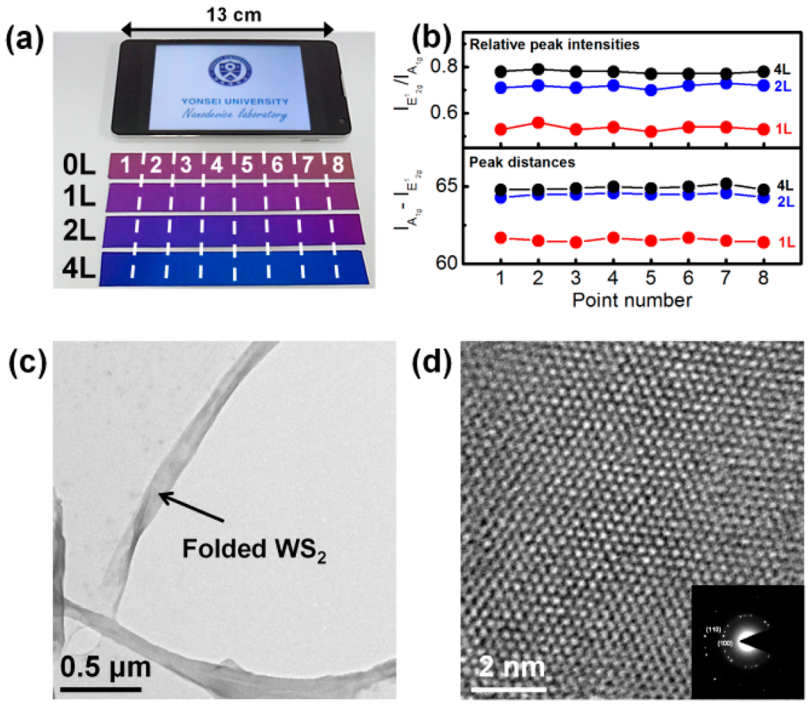

Figure 3. (a) Large-area (approximately 13 cm) mono-, bi-, and tetralayer WS_2 nanosheets on SiO_2 substrates (at a size comparable to a cellular phone display screen), (b) relative Raman peak intensities (upper) and peak distances (bottom) of the E^1_{2g} and A_{1g} bands for eight measurement points on the mono- (red), bi- (blue), and tetralayer (black) WS_2 nanosheets, (c) low-magnification TEM image for a monolayer WS_2 nanosheet on a TEM grid, (d) a HRTEM image of a monolayer WS_2 nanosheet at a selected region, and (inset) the SAED pattern of the polycrystalline monolayer WS_2 nanosheet.

the relative Raman peak intensities and distances vary with the number of layers, from 0.5 to 0.8 and from 61.5 to 65 cm^{-1}, respectively, as shown in Figure 2. This result confirms good uniformity and thickness control for the ALD-based WS_2 nanosheet, up to the 6 in. wafer length scale.

The crystallinity of the ALD-based monolayer WS_2 nanosheet was evaluated using high-resolution TEM (HRTEM). Figure 3c shows a low-magnification TEM image of a folded region of the transferred WS_2 nanosheet on a TEM grid, which formed during TEM sample preparation. The HRTEM image in Figure 3d shows periodically arranged atoms at the selected region of the ALD-based monolayer WS_2 nanosheet. A honeycomb-like structure and 6-fold coordination symmetry are observed in the fast Fourier transformation (FFT) image (Figure S3). The selected-area electron diffraction (SEAD) patterns of the ALD-based monolayer WS_2 nanosheet (shown in the inset of Figure 3d) taken with an approximately 30 nm aperture size indicates a polycrystalline crystal structure and diffraction points of (100) and (110).[12] The approximate grain size is 10−20 nm, which is similar to that of MoS_2 nanosheet synthesized by sulfurization of Mo thin film.[42]

To evaluate the electrical performance of the ALD-based monolayer WS_2 nanosheet, we fabricated a top-gate FET on the WS_2/SiO_2 substrate by evaporating Au(60 nm)/Ti(5 nm) electrodes and an ALD HfO_2 (50 nm) gate insulator through conventional photolithography and reactive ion (O_2 plasma) etching processes, as shown in Figure 4a. Figure 4b shows the characteristics measured at room temperature in air. The field-effect electron mobility was extracted from the linear regime of the transfer curve using the equation $\mu = (\Delta I_d/\Delta V_g) \times L/(WC_{ox}V_d)$, where L, W, and C_{ox} are the channel length, channel width, and gate capacitance per unit area, respectively. The extracted field effect electron mobility is 3.9 $cm^2/V \cdot s$, which is much higher than the previously reported value for a CVD WS_2 FET device (approximately 0.01 $cm^2/V \cdot s$).[40] This result shows that our WS_2 nanosheet is of good quality, which is required for electronic devices. The significant improvement in the field-effect mobility of the current device is partially due to the dielectric screening effect from the high-k dielectric gate insulator.[5,51] Furthermore, the subthreshold swing (SS) value is as low as 0.6 V/dec, which is comparable to that of an FET device fabricated using exfoliated MoS_2.[16] Notably, this is the first FET with a high-k dielectric gate insulator prepared using a synthesized WS_2 nanosheet.

One of the most important advantages of the ALD process is its excellent conformality. Thus, the ALD process can conformally deposit films on complex structures such as trenches and NWs. On the basis of the high conformality of the ALD process, we have also developed a novel process to fabricate WS_2 nanotubes (WNTs). Figure 5a shows the process scheme for fabricating WS_2 nanotubes. Aligned Si NWs were oxidized at 1000 °C for 1 h in O_2 ambient to form a SiO_2 layer. A WO_3 film was conformally deposited by 50 cycles of PE-ALD on the SiO_2/Si NWs, which was followed by a sulfurization

process to form WS_2. After sulfurization, the $WS_2/SiO_2/Si$ NWs were immersed in HF solution to etch the SiO_2 layer, which resulted in isolated WNTs.

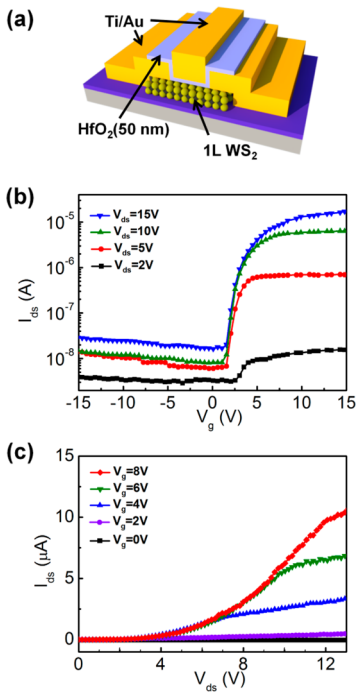

Figure 4. (a) FET structure on the monolayer WS_2, (b) transfer curve for the FET fabricated on a monolayer WS_2 nanosheet, and (c) output curve for the FET fabricated on a monolayer WS_2 nanosheet.

The scanning electron microscopy (SEM) images for each procedure are shown in the Supporting Information (Figure S4). Figure 5b shows an SEM image of the WNTs after the SiO_2 sample was transferred. The WNTs appear to be transparent due to the atomically thin structure, as indicated by arrows. Figure 5c shows a low-magnification TEM image of a WNT on a TEM grid. The WNT has a diameter of approximately 400 nm, replicating the diameter of the Si NW template. A relatively large surface roughness is seen for the WTNs as a result of the large surface roughness of the SiO_2/Si NWs. The HRTEM image for the region denoted by a red circle of WNTs (Figure 5d) clearly shows the formation of tetralayer WS_2 with an interlayer spacing of 0.65 nm, which is consistent with planar WS_2. Chemical composition analysis of a WNT was conducted using high-angle annular dark-field (HAADF) and energy-dispersive X-ray spectrometry (EDX) elemental mapping of the W and S (Figure 5e−g). The HAADF image shows a torn region on the WNT surface that appeared during the TEM sample preparation. The element maps corresponding to the W and S confirm the presence of WNTs, which is further supported by the Raman spectroscopy result (Figure S4(e)). In previous reports, the WNTs were synthesized using sulfurization of WO_3 nanowhiskers and nanoneedles. However, it is difficult to control the geometry of the WNTs, such as diameter, length and number of layers, by those methods.[47,48] In contrast, for the current WNT fabrication method based on ALD and nanotemplates, it is relatively easy to control

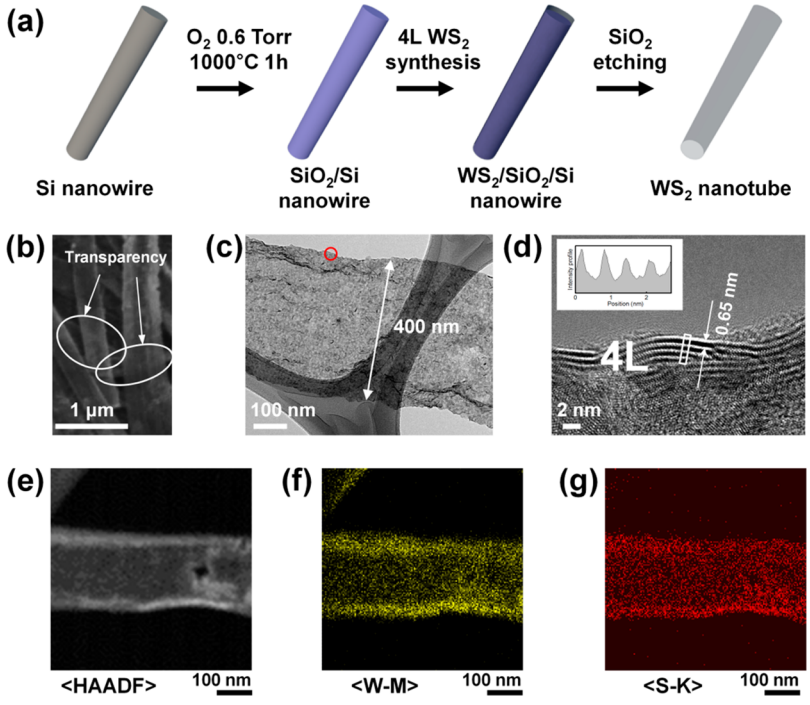

Figure 5. (a) Synthesis procedure for the WNTs, (b) SEM image of the WNTs and (inset) crossed WNTs, (c) a low-magnification TEM image of an individual WNT on a TEM grid, (d) a HRTEM image of the edge of the tetralayer WNT (red circle in (c)) and (inset) the intensity profile of the region denoted by the solid line, (e) a HAADF TEM image of an individual WNT on a TEM grid, and EDX elemental maps of (f) W and (g) S in the HAADF image.

the diameter, length, and number of layers of the WNTs. It should be noted that the current processing scheme is not limited to Si NWs; numerous other nanotemplates, including NWs, nanoparticles, and nanohole structures could be exploited. Thus, our conformal and systematic layer-control synthesis method for WS_2 is expected to be applicable to various multidimensional nanostructures.

CONCLUSION

In summary, we have reported an ALD-based WS_2 synthesis process based on the sulfurization of highly pure PE-ALD WO_3 films. We demonstrated that the ALD-based WS_2 nanosheet synthesis process has a systematic layer controllability and wafer-level uniformity. The fabricated WS_2-based top-gate FET exhibited high field-effect electron mobility of approximately 3.9 $cm^2/V \cdot s$ and a low SS of 0.6 V/dec Moreover, we demonstrated that the high conformality of the ALD-based WS_2 synthesis process enables the fabrication of WNTs using nanotempates. It should be noted that the ALD-based TMDC synthesis process is not limited to WS_2. We expect similar process schemes can be developed for other TMDC materials.

EXPERIMENTAL SECTION

WO_3 Film Growth. A 6 in. ALD chamber with a loadlock chamber was used for the deposition of the WO_3 films. The WO_3 films were deposited onto SiO_2/Si substrates using a newly synthesized precursor, $WH_2(iPrCp)_2$, and O_2 plasma at a 300 °C growth temperature. The temperature of the bubbler containing $WH_2(iPrCp)_2$ was kept at 95 °C for adequate vapor pressure, and vaporized $WH_2(iPrCp)_2$ molecules were carried into the chamber by pure argon (99.999%) carrier gas. The O_2 flow and plasma power were fixed at 300 sccm and 200 W, respectively. An ALD cycle consists of four steps: $WH_2(iPrCp)_2$ precursor exposure (t_s), Ar purging (t_p), O_2 plasma reactant exposure (t_r), and another Ar purging (t_p). In the PE-ALD WO_3 process, the t_s, t_p, and t_r were fixed at 5, 12, and 5 s, respectively. Optimization of PE-ALD WO_3 process is described in the Supporting Information (Figure S1).

Sulfurization of WO_3 Film. To the sulfurization of WO_3 film, the WO_3 deposited on the SiO_2/Si substrate was placed in the center of a tube furnace (1.2 in. in diameter). Initially, the sample was heated to 470 °C for 60 min under flowing H_2 (25 sccm) and Ar (25 sccm) gas to remove any organic contaminants on the surface. Second, the temperature was gradually increased from 470 to 1000 °C over a period of 90 min and was maintained at 1000 °C for 30 min with flowing Ar (50 sccm) and H_2S (5 sccm). The sample was subsequently cooled to room temperature under a flowing Ar (50 sccm) atmosphere.

Transfer of WS_2 Nanosheet. As-synthesized WS_2 nanosheet on the SiO_2 substrate was coated with polymethyl methacrylate (PMMA) by spin coating at 4000 rpm for 60 s. After curing the PMMA at 100 °C for 15 min, the sample was immersed in 10% HF solution in order to etch the SiO_2 layer. Subsequently, the sample was washed out by DI water and scooped onto a clean SiO_2/Si substrate. The PMMA was removed by acetone and washed out by isopropyl alcohol.

WS_2 Nanotubes Fabrication. Aligned Si NWs were fabricated using gold-assisted chemical etching method[52] and oxidized in O_2 ambient (0.6 Torr) at 1000 °C for 1 h to form a SiO_2 layer on the Si NWs surface. A WO_3 film was deposited (50 cycles) by PE-ALD on the SiO_2/Si NWs which have diameter of 400 nm and length of a few micrometers. Subsequently, WO_3/SiO_2/Si NWs were sulfurized to form WS_2/SiO_2/Si NWs array. WS_2/SiO_2/Si NWs were immersed in 10% HF solution to etch the SiO_2 layer. Then, sample was immersed in DI water to float the WNT on the surface of DI water, and new SiO_2/Si substrate was used to fish the floating WNTs.

Characterization of WS_2 Nanosheets and Nanotubes. OM (Olympus DX51), Raman spectroscopy (HORIBA, Lab Ram ARAMIS; 633 nm laser excitation wavelength), AFM (VEECO, Multimode), PL (SPEX1403, SPEX; 532 nm laser excitation wavelength), XPS (Thermo U. K, K-alpha), SEM (JEOL Ltd., JSM-6701F), TEM, and EDX (Tecnai G2 F20 S-TWIN; accelerating voltage, 200 kV) were employed to characterize the WS_2 nanosheets and nanotubes.

Conflict of Interest: The authors declare no competing financial interest.

Supporting Information Available: PE-ALD WO_3 thin films and process optimization; WS_2 nanosheets fabricated using various ALD cycle numbers of WO_3; crystal direction of WS_2; and ALD-based WS_2 nanotubes. This material is available free of charge *via* the Internet at http://pubs.acs.org.

Acknowledgment. This research was supported by the Converging Research Center Program through the Ministry of Education, Science and Technology (2013K000173) and the Industrial Strategic Technology Development Program (10041926, Development of high density plasma technologies for thin film deposition of nanoscale semiconductor and flexible display processing) funded by the Ministry of Knowledge Economy (MKE, Korea).

REFERENCES AND NOTES

1. Ramakrishna Matte, H. S. S.; Gomathi, A.; Manna, A. K.; Late, D. J.; Datta, R.; Pati, S. K.; Rao, C. N. R. MoS_2 and WS_2 Analogues of Graphene. *Angew. Chem.* **2010**, *122*, 4153–4156.
2. Wang, Q. H.; Kalantar-Zadeh, K.; Kis, A.; Coleman, J. N.; Strano, M. S. Electronics and Optoelectronics of Two-Dimensional Transition Metal Dichalcogenides. *Nat. Nanotechnol.* **2012**, *7*, 699–712.
3. Novoselov, K. S.; Jiang, D.; Schedin, F.; Booth, T. J.; Khotkevich, V. V.; Morozov, S. V.; Gein, A. K. Two-Dimensional Atomic Crystals. *Proc. Natl. Acad. Sci. U.S.A.* **2005**, *102*, 10451–10453.
4. Chhowalla, M.; Shin, H. S.; Eda, G.; Li, L.-J.; Loh, K. P.; Zhang, H. The Chemistry of Two-Dimensional Layered Transition Metal Dichalcogenide Nanosheets. *Nat. Chem.* **2013**, *5*, 263–275.
5. Radisavljevic, B.; Radenovic, A.; Brivio, J.; Giacometti, V.; Kis, A. Single-Layer MoS_2 Transistors. *Nat. Nanotechnol.* **2011**, *6*, 147–150.
6. Baugher, B. W. H.; Churchill, H. O. H.; Yang, Y.; Jarillo-Herrero, P. Intrinsic Electronic Transport Properties of High-Quality Monolayer and Bilayer MoS_2. *Nano Lett.* **2013**, *13*, 4212–4216.
7. Levi, R.; Bitton, O.; Leitus, G.; Tenne, R.; Joselevich, E. Field-Effect Transistors Based on WS_2 Nanotubes with High Current-Carrying Capacity. *Nano Lett.* **2013**, *13*, 3736–3741.
8. Zhang, C.; Ning, Z.; Liu, Y.; Xu, T.; Guo, Y.; Zak, A.; Zhang, Z.; Wang, S.; Tenne, R.; Chen, Q. Electrical Transport Properties of Individual WS_2 Nanotubes and Their Dependence on Water and Oxygen Absorption. *Appl. Phys. Lett.* **2012**, *101*, 113112–113115.
9. Mak, K. F.; Lee, C.; Hone, J.; Shan, J.; Heinz, T. F. Atomically Thin MoS_2: A New Direct-Gap Semiconductor. *Phys. Rev. Lett.* **2010**, *105*, 136805−1–4.
10. Seiferta, G.; Terrones, H.; Terrones, M.; Jungnickel, G.; Frauenheim, T. On the Electronic Structure of WS_2 Nanotubes. *Solid State Commun.* **2000**, *114*, 245–248.
11. Seifert, G.; Terrones, H.; Terrones, M.; Jungnickel, G.; Frauenheim, T. Structure and Electronic Properties of MoS_2 Nanotubes. *Phys. Rev. Lett.* **2000**, *85*, 146–149.

12. Gutiérrez, H. R.; Perea-López, N.; Elías, A. L.; Berkdemir, A.; Wang, B.; Lv, R.; López-Urías, F.; Crespi, V. H.; Terrones, H.; Terrones, M. Extraordinary Room-Temperature Photoluminescence in Triangular WS_2 Monolayers. *Nano Lett.* **2013**, *13*, 3447–3454.
13. Eda, G.; Yamaguchi, H.; Voiry, D.; Fujita, T.; Chen, M.; Chhowalla, M. Photoluminescence from Chemically Exfoliated MoS_2. *Nano Lett.* **2011**, *11*, 5111–5116.
14. Sundaram, R. S.; Engel, M.; Lombardo, A.; Krupke, R.; Ferrari, A. C.; Avouris, P.; Steiner, M. Electroluminescence in Single Layer MoS_2. *Nano Lett.* **2013**, *13*, 1416–1421.
15. Perea-López, N.; Elías, A. L.; Berkdemir, A.; Castro-Beltran, A.; Gutiérrez, H. R.; Feng, S.; Lv, R.; Hayashi, T.; López-Urías, F.; Ghosh, S.; Muchharla, B.; *et al.* Photosensor Device Based on Few-Layered WS_2 Films. *Adv. Funct. Mater.* **2013**, 10.1002/adfm.201300760.
16. Lee, H. S.; Min, S.-W.; Chang, Y.-G.; Park, M. K.; Nam, T.; Kim, H.; Kim, J. H.; Ryu, S.; Im, S. MoS_2 Nanosheet Phototransistors with Thickness-Modulated Optical Energy Gap. *Nano Lett.* **2012**, *12*, 3695–3700.
17. Zhang, C.; Wang, S.; Yang, L.; Liu, Y.; Xu, T.; Ning, Z.; Zak, A.; Zhang, Z.; Tenne, R.; Chen, Q. High-Performance Photodetectors for Visible and Near-Infrared Lights Based on Individual WS_2 Nanotubes. *Appl. Phys. Lett.* **2012**, *100*, 243101–243105.
18. Han, S. W.; Hwang, Y. H.; Kim, S.-H.; Yun, W. S.; Lee, J. D.; Park, M. G.; Ryu, S.; Park, J. S.; Yoo, D.-H.; Yoon, S.-P.; *et al.* Controlling Ferromagnetic Easy Axis in a Layered MoS_2 Single Crystal Sang. *Phys. Rev. Lett.* **2013**, *110*, 247201.
19. Lu, P.; Wu, X.; Guo, W.; Zeng, X. C. Strain-Dependent Electronic and Magnetic Properties of MoS_2 Monolayer, Bilayer, Nanoribbons and Nanotubes. *Phys. Chem. Chem. Phys.* **2012**, *14*, 13035–13040.
20. Liu, H.; Su, D.; Wang, G.; Qiao, S. Z. An Ordered Mesoporous WS_2 Anode Material with Superior Electrochemical Performance for Lithium Ion Batteries. *J. Mater. Chem.* **2012**, *22*, 17437–17440.
21. Wang, J.-Z.; Lu, L.; Lotya, M.; Coleman, J. N.; Chou, S.-L.; Liu, H.-K.; Minett, A. I.; Chen, J. Development of MoS_2–CNT Composite Thin Film from Layered MoS_2 for Lithium Batteries. *Adv. Energy Mater.* **2013**, *3*, 798–805.
22. Hwang, H.; Kim, H.; Cho, J. MoS_2 Nanoplates Consisting of Disordered Graphene-Like Layers for High Rate Lithium Battery Anode Materials. *Nano Lett.* **2011**, *11*, 4826–4830.
23. Liang, Y.; Feng, R.; Yang, S.; Ma, H.; Liang, J.; Chen, J. Rechargeable Mg Batteries with Graphene-Like MoS_2 Cathode and Ultrasmall Mg Nanoparticle Anode. *Adv. Mater.* **2011**, *23*, 640–643.
24. Voiry, D.; Yamaguchi, H.; Li, J.; Silva, R.; Alves, D. C. B.; Fujita, T.; Chen, M.; Asefa, T.; Shenoy, V. B.; Eda, G.; *et al.* Enhanced Catalytic Activity in Strained Chemically Exfoliated WS_2 Nanosheets for Hydrogen Evolution. *Nat. Mater.* **2013**, *12*, 850–855.
25. Yun, W. S.; Han, S. W.; Hong, S. C.; Kim, I. G.; Lee, J. D. Thickness and Strain Effects on Electronic Structures of Transition Metal Dichalcogenides: 2H-MX_2 Semiconductors (M = Mo, W; X = S, Se, Te). *Phys. Rev. B* **2012**, *85*, 033305.
26. Peelaers, H.; Van de Walle, C. G. Effects of Strain on Band Structure and Effective Masses in MoS_2. *Phys. Rev. B* **2012**, *86*, 241401.
27. Mak, K. F.; He, K.; Shan, J.; Heinz, T. F. Control of Valley Polarization in Monolayer MoS_2 by Optical Helicity. *Nat. Nanotechnol.* **2012**, *7*, 494–498.
28. Zeng, H.; Dai, J.; Yao, W.; Xiao, D.; Cui, X. Valley Polarization in MoS_2 Monolayers by Optical Pumping. *Nat. Nanotechnol.* **2012**, *7*, 490–493.
29. Zhao, W.; Ghorannevis, Z.; Chu, L.; Toh, M.; Kloc, C.; Tan, P.-H.; Eda, G. Evolution of Electronic Structure in Atomically Thin Sheets of WS_2 and WSe_2. *ACS Nano* **2012**, *7*, 791–797.
30. Zeng, H.; Liu, G.-B.; Dai, J.; Yan, Y.; Zhu, B.; He, R.; Xie, L.; Xu, S.; Chen, X.; Yao, W. Optical Signature of Symmetry Variations and Spin-Valley Coupling in Atomically Thin Tungsten Dichalcogenides. *Sci. Rep.* **2013**, *3*, 1608.
31. Wang, H.; Yu, L.; Lee, Y.-H.; Fang, W.; Hsu, A.; Herring, P.; Chin, M.; Dubey, M.; Li, L.-J.; Kong, J.; *et al.* Large-Scale 2D Electronics based on Single-Layer MoS_2 Grown. *IEEE Int. Electron Devices Meet.* **2012**, 4.6.1–4.6.4.
32. Radisavljevic, B.; Whitwick, M. B.; Kis, A. Integrated Circuits and Logic Operations Based on Single-Layer MoS_2. *ACS Nano* **2011**, *5*, 9934–9938.
33. Wang, H.; Yu, L.; Lee, Y.-H.; Shi, Y.; Hsu, A.; Chin, M. L.; Li, L.-J.; Dubey, M.; Kong, J.; Palacios, T. Integrated Circuits Based on Bilayer MoS_2 Transistors. *Nano Lett.* **2012**, *12*, 4674–4680.
34. Bernardi, M.; Palummo, M.; Grossman, J. C. Extraordinary Sunlight Absorption and One Nanometer Thick Photovoltaics Using Two-Dimensional Monolayer Materials. *Nano Lett.* **2013**, *13*, 3664–3670.
35. Eda, G.; Maier, S. A. Two-Dimensional Crystals: Managing Light for Optoelectronics. *ACS Nano* **2013**, *7*, 5660–5665.
36. Nicolosi, V.; Chhowalla, M.; Kanatzidis, M. G.; Strano, M. S.; Coleman, J. N. Liquid Exfoliation of Layered Materials. *Science* **2013**, *340*, 6139.
37. Liu, K.-K.; Zhang, W.; Lee, Y.-H.; Lin, Y.-C.; Chang, M.-T.; Su, C.-Y.; Chang, C.-S.; Li, H.; Shi, Y.; Zhang, H.; *et al.* Growth of Large-Area and Highly Crystalline MoS_2 Thin Layers on Insulating Substrates. *Nano Lett.* **2012**, *12*, 1538–1544.
38. Lee, Y.-H.; Zhang, X.-Q.; Zhang, W.; Chang, M.-T.; Lin, C.-T.; Chang, K.-D.; Yu, Y.-C.; Wang, J. T.-W.; Chang, C.-S.; Li, L.-J.; *et al.* Synthesis of Large-Area MoS_2 Atomic Layers with Chemical Vapor Deposition. *Adv. Mater.* **2012**, *24*, 2320–2325.
39. van der Zande, A. M.; Huang, P. Y.; Chenet, D. A.; Berkelbach, T. C.; You, Y.; Lee, G.-H.; Heinz, T. F.; Reichman, D. R.; Muller, D. A.; Hone, J. C. Grains and Grain Boundaries in Highly Crystalline Monolayer Molybdenum Disulphide. *Nat. Mater.* **2013**, *12*, 554–561.
40. Lee, Y.-H.; Yu, L.; Wang, H.; Fang, W.; Ling, X.; Shi, Y.; Lin, C.-T.; Huang, J.-K.; Chang, M.-T.; Chang, C.-S.; *et al.* Synthesis and Transfer of Single-Layer Transition Metal Disulfides on Diverse Surfaces. *Nano Lett.* **2013**, *13*, 1852–1857.
41. Zhang, Y.; Zhang, Y.; Ji, Q.; Ju, J.; Yuan, H.; Shi, J.; Gao, T.; Ma, D.; Liu, M.; Chen, Y.; *et al.* Controlled Growth of High-Quality Monolayer WS_2 Layers on Sapphire and Imaging Its Grain Boundary. *ACS Nano* **2013**, *7*, 8963–8971.
42. Zhan, Y.; Liu, Z.; Najmaei, S.; Ajayan, P. M.; Lou, J. Large-Area Vapor-Phase Growth and Characterization of MoS_2 Atomic Layers on a SiO_2 Substrate. *Small* **2012**, *8*, 966–971.
43. Lin, Y.-C.; Zhang, W.; Huang, J.-K.; Liu, K.-K.; Lee, Y.-H.; Liang, C.-T.; Chu, C.-W.; Li, L.-J. Wafer Scale MoS_2 Thin Layers Prepared by MoO_3 Sulfurization. *Nanoscale* **2012**, *4*, 6637–6641.
44. Elías, A. L.; Perea-López, N.; Castro-Beltrán, A.; Berkdemir, A.; Lv, R.; Feng, S.; Long, A. D.; Hayashi, T.; Kim, Y. A.; Endo, M.; Gutiérrez, H. R.; *et al.* Controlled Synthesis and Transfer of Large-Area WS_2 Sheets: From Single Layer to Few Layers. *ACS Nano* **2013**, *7*, 5235–5242.
45. Kim, H. Characteristics and Applications of Plasma Enhanced-Atomic Layer Deposition. *Thin Solid Films* **2011**, *519*, 6639–6644.
46. Kim, H.; Lee, H.-B.-R.; Maeng, W. J. Applications of Atomic Layer Deposition to Nanofabrication and Emerging Nanodevices. *Thin Solid Films* **2009**, *517*, 2563–2580.
47. Remškar, M. Inorganic Nanotubes. *Adv. Mater.* **2004**, *16*, 1497–1504.
48. Zak, A.; Sallacan-Ecker, L.; Margolin, A.; Feldman, Y.; Popovitz-Biro, R.; Albu-Yaron, A.; Genut, M.; Tenne, R. Scaling Up of the WS_2 Nanotubes Synthesis. *Fullerenes, Nanotubes, Carbon Nanostruct.* **2011**, *19*, 18–26.
49. Berkdemir, A.; Gutiérrez, H. R.; Botello-Méndez, A. R.; Perea-López, N.; Elías, A. L.; Chia, C.-I.; Wang, B.; Crespi, V. H.; López-Urías, F.; Charlier, J.-C. Identification of Individual and Few Layers of WS_2 Using Raman Spectroscopy. *Sci. Rep.* **2013**, *3*, 1755.

50. Molina-Sánchez, A.; Wirtz, L. Phonons in Single-Layer and Few-Layer MoS_2 and WS_2. *Phys. Rev. B* **2011**, *84*, 155413.
51. Yoon, Y.; Ganapathi, K.; Salahuddin, S. How Good Can Monolayer MoS_2 Transistors Be? *Nano Lett.* **2011**, *11*, 3768–3773.
52. Mikhael, B.; Elise, B.; Xavier, M.; Sebastian, S.; Johann, M.; Laetitia, P. New Silicon Architectures by Gold-Assisted Chemical Etching. *ACS Appl. Mater. Interfaces* **2011**, *3*, 3866–3873.